Journal of the Physical Society of Japan
Vol. 73, No. 12, December, 2004, pp. 3370–3377

Aharonov–Bohm-type Effects in Triangular Antidot Lattice

Yaushiro IYE*, Masaaki UEKI, Akira ENDO and Shingo KATSUMOTO

Institute for Solid State Physics, University of Tokyo, 5-1-5 Kashiwanoha, Kashiwa, Chiba 277-8581

(Received August 10, 2004)

Three kinds of Aharonov–Bohm (AB)-type oscillation have been investigated in triangular antidot lattice fabricated from a GaAs/AlGaAs two-dimensional electron gas sample. The oscillation periods of Altshuler–Aronov–Spivak (AAS) effect and AB-type effect near zero magnetic field are determined by the unit cell area, whereas those of AB-type oscillations in the quantum Hall plateau transition regime are governed by the effective area of antidot. The evolution of the high-field AB-type oscillation as a function of gate voltage gives infomation on the profile of the self-consistent potential associated with compressible edge channels formed around antidot. The temperature dependences and decoherence mechanisms of the AAS and AB-type oscillations near zero magnetic field as well as the high-field AB-type oscillation are discussed.

KEYWORDS: Aharonov–Bohm effect, antidot lattice, GaAs/AlGaAs, edge channel, decoherence
DOI: 10.1143/JPSJ.73.3370

1. Introduction

Aharonov–Bohm (AB) effect[1] manifests itself in a wide range of quantum interference phenomena in mesoscopic electron systems, and offers a powerful means to probe electronic phase coherence. The first experimental evidence of the AB effect (in a wider sense) in mesoscopic transport was obatained by observation of magnetoresistance oscillation with periodicity $h/2e$ in small metal cylinder.[2] This effect was attributed to interference between time-reversed pair of electron waves and was called Altshuler–Aronov–Spivak (AAS) effect.[3] Observation of the AB oscillation (in its narrower sense) with periodicity h/e was subsequently achieved in a small metal ring with large aspect ratio.[4] These pioneering experiments were performed on mesoscocpic strucrures made of metals where electron transport was diffusive. The AAS and AB effects were then observed in mesoscopic structures based on semiconductor two-dimensional gas (2DEG) systems where electron transport was ballistic or quasi-ballistic.[5] Similar quantum oscillation phenomena were also observed in antidot lattices, i.e., periodically perforated 2DEG system. The first observation of the AB oscillation in antidot lattice was made by Nihey *et al.*[6] and by Weiss *et al.*[7] They detected B-periodic small oscillations superposed on the commensurability peak of magnetoresistance in square antidot lattices. Later, the AAS oscillation was observed in triangular antidot lattice.[8]

Antidot lattice can be viewed as a network consisting of many loops. Studies on normal metal rings have established the essential difference between the AAS effect and AB effect in their response to ensemble averaging. The amplitude of AB oscillation diminishes by ensemble averaging, because the relative phase of two interfering electron waves differs from one ring to another.[9] By contrast, the AAS effect, whose origin lies in the interefference between time-reversed pair of electron waves, is immune to ensemble averaging. Thus, the very fact that AB oscillation could be observed in antidot lattice of macroscopic overall size, was rather surprising. Subsequent theoretical studies have attributed the effect to oscillatory fine structure of the density of state spectra, as calculated for instance by periodic orbit theory.[10] For this reason, it is customary to call the effect AB-*type* oscillation so as to distinguish it from the ordinary AB effect in the single ring case. There is an intermediate case of finite antidot lattices,[13] in which a small number of antidots constitute a mesoscopic size system that becomes phase coherent as a whole at low enough temperatures. Despite much theoretical work,[10–12] full understanding of the physical origin of the AB-type oscillation in macroscopic antidot lattice is yet to be worked out.

In the present work, we investigate the AAS and AB-type oscillations in triangular antidot lattices both near zero magnetic field and in high fields. Figure 1 schematically shows the potential landscape for electrons in a triangular antidot lattice. We study how the AB-type oscillation behaves in different field ranges and how it changes with gate voltage. We also study the temperature dependences of the different types of oscillation, and discuss them in comparison with those seen in single ring systems.[14,15]

2. Experimental

The samples were fabricated from a GaAs/AlGaAs single heterojunction wafer with electron density $n = 3.6 \times 10^{15}\,\mathrm{m}^{-2}$ and mobility $\mu = 68\,\mathrm{m}^2/(\mathrm{V\,s})$. The hetero-interface was located 60 nm deep from the surface. The electron mean free path at low temperatures was $\sim$6 μm. Samples were mesa-etched into a standard Hall bar shape with AuGe

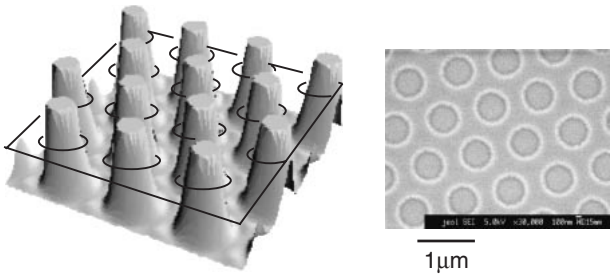

Fig. 1. Schematic potential landscape of triangular antidot lattice. The picture on the right is a scanning electron micrograph of the antidot lattice sample.

*E-mail: iye@issp.u-tokyo.ac.jp

ohmic contact pads. The triangular pattern of antidots was created on the active part of the Hall bar by electron beam lithography and wet chemical etching. The lattice parameter was $a = 960\,\mathrm{nm}$ and the aspect ratio d/a (d being the antidot diameter) was 0.6 for sample #1 and 0.7 for sample #2. Due to the finite width of depletion region on the order of 100 nm, the effective diameter d^* of antidot was larger than the lithographical value d by an amount which depended on the carrier density. The length scale of the present antidot lattice sample was somewhat larger than those previously studied,[6,8,16–19] which made it possible to obtain good lithographical regularity and uniformity as seen from the scanning electron micrograph shown in Fig. 1.

The antidot array fully covered the active area of the Hall bar. The rectangular area ($46 \times 177\,\mu\mathrm{m}^2$) between the voltage probes contained $\sim 10^4$ antidots. The samples were equipped with a Au–Ti Schottky front gate which controlled the 2DEG density over the range $n = (1.5\text{–}4) \times 10^{15}\,\mathrm{m}^{-2}$. The values of low temperature resisitivity at zero magnetic field and at zero gate bias were 1.2 kΩ (#1) and 3.9 kΩ (#2), respectively, which indicated that the conducting path between the antidots contained several 1D channels. Magnetoresistance and Hall resistance were measured by a standard low frequency *ac* technique at dilution refrigerator temperatures in a 15-T magnet.

3. Results and Discussion

3.1 AAS and AB-type oscillations near zero magnetic field

Figure 2 shows magnetoresistance traces of sample #2 taken at 30 mK for different settings of gate voltage V_G. With decreasing carrier density, the resistivity at zero magnetic field increases sharply, while the behavior at magnetic fields above 1 T only changes gradually. The data for sample #1 having a smaller aspect ratio look similar to this figure except that the resistivity at zero magnetic field is lower. The large negative magnetoresistance at low field is one of the characteristic features of transport in triangular antidot lattice.[8]

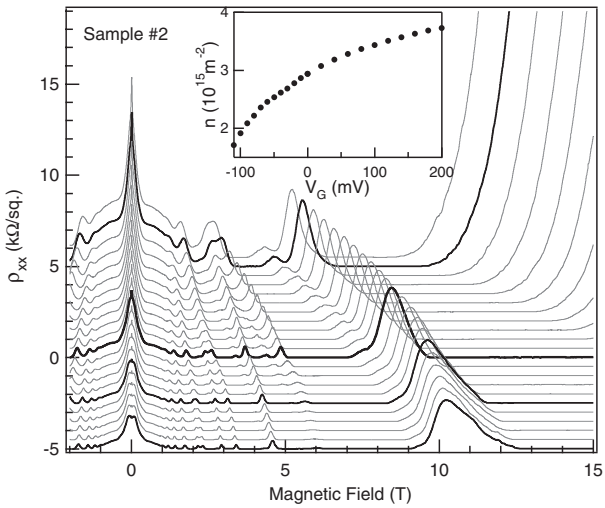

Fig. 2. The inset shows the dependence of 2DEG density on the gate voltage V_G in sample #2. The main panel shows magnetoresistance traces taken at 30 mK for different settings of V_G ranging from -110 mV (*top*) to $+200$ mV (*bottom*). Each trace is vertically offset by 0.5 kΩ for clarity. Thick curves correspond to $V_G = +200$, $+100$, 0 and -100 mV, respectively.

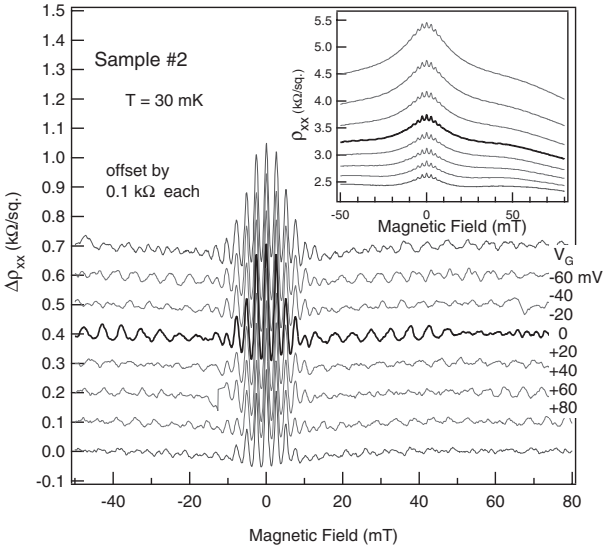

Fig. 3. The inset shows the traces in the low magnetic field range. Each curve in the main panel shows oscillatory part after a smooth background has been subtracted. The rapid oscillation around zero magnetic field is the AAS ($h/2e$) effect. The oscillation seen at somewhat higher fields is the AB-type (h/e) oscillation. The thick curves are the data for $V_G = 0$.

We first focus on the low field region. The inset of Fig. 3 presents an expanded view of the traces in the low magnetic field range. Magnetoresistance oscillation around zero magnetic field is clearly identified. The main panel of Fig. 3 shows the oscillatory part obtained by subtracting a smooth background. In addition to the rapid oscillation around zero magnetic field, a slower oscillation at somewhat higher fields is distinctly visible in this plot. The amplitude of the rapid oscillation diminishes steeply with magnetic field. On the other hand, the slower oscillation is best visible in the field range which roughly corresponds to the "shoulder" of the negative magnetoresistance.

Fourier power spectra of these traces are shown in Fig. 4. The spectra in the upper panel of Fig. 4 are obtained from the data in the field range $-20 < B < 20\,\mathrm{mT}$, where the rapid oscillation dominates. The primary peak is located at $390\,\mathrm{T}^{-1}$ and its second harmonic is visible. The oscillation period 2.6 mT agrees very well with the expected period of the AAS oscillation, $h/2eS = 2.59\,\mathrm{mT}$ evaluated with the loop area S taken to be the unit cell area $(\sqrt{3}/2)a^2 = 0.80\,\mu\mathrm{m}^2$ of the triangular lattice. The lower panel shows Fourier spectra taken from the data in the field range $20 < B < 100\,\mathrm{mT}$. The primary peak resides at $\sim 200\,\mathrm{T}^{-1}$ and its harmonics up to the fourth order are discernible. The period ~ 5 mT is consistent with the expected period of the AB-type oscillation, $h/eS = 5.18\,\mathrm{mT}$.

As seen in Figs. 3 and 4, the periods of the AAS and AB-type oscillations at low field are fixed by the unit cell area of the triangular lattice and are unaffected by the gate voltage. This is in contrast to the AB-type oscillation at high fields to be discussed in the next subsection. It is noted that the amplitude of the AB-type oscillation varies more sensitively with V_G than that of the AAS-oscillation.

The typical amplitude of the AB-type conductance oscillation observed here is $\sim(0.01\text{–}0.05)e^2/h$. In comparison with the AB oscillation in ballistic single ring systems

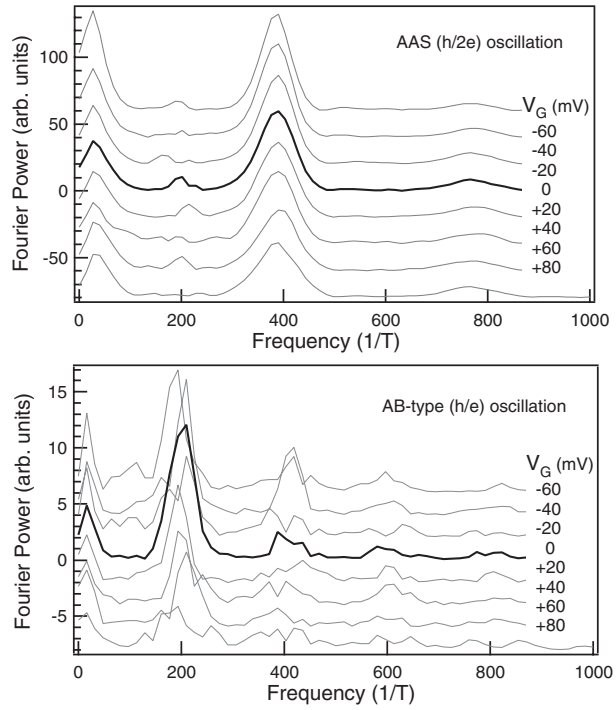

Fig. 4. Fourier power spectra obtained from the traces in Fig. 3. The spectra on the upper panel are calculated from the data in the range $-20 < B < 20$ mT, while those on the lower panel are from $20 < B < 100$ mT. The thick curves are the data for $V_G = 0$.

whose amplitude ranges over $(0.01–1)e^2/h$ among literatures,[5,14,15] this is a fairly large value. The observation of AB-type oscillation with substantial amplitude testifies the lithographic regularity of the present system. It also poses a question concerning the physical origin of the effect mentioned in the introduction. We shall come back to this issue in a later section.

3.2 AB-type oscillation in quantum Hall regime

A different kind of AB-type oscillation is observed in higher magnetic fields. Figure 5 shows magnetoresistance traces of sample #2 in field range $3.6 < B < 3.9$ T, which corresponds to the quantum Hall plateau transition between $\nu = 4$ and 3. The inset shows the oscillatory part obtained by subtraction of smooth background. Resistance oscillation periodic in B is clearly identified, which we call high-field AB-type oscillation (HFABO) hereafter. Likewise, we shall use a term LFABO for the low-field AB-type oscillation presented in the preceding subsection. The amplitude of HFABO is largest near the resistance peak in this figure.

Figure 6(a) shows the Fourier power spectra of the HFABO around $\nu \sim 3.5$ taken at different gate voltages (accordingly different field ranges). While the period of LFABO corresponds to a flux quantum per unit cell area, the HFABO period takes a larger value corrensponding to a smaller loop area. The loop area calculated from the HFABO period turns out to be consistent with the antidot area $(\pi/4)d^{*2}$ (with appropriate allowance for depletion region). This fact indicates that edge channels encircling the antidots are responsible for the HFABO.

Figure 6(b) presents the global evolution of the Fourier spectrum of HFABO at $\nu \sim 3.5$ with the gate voltage as a gray scale plot. Toward the negative gate voltage (lower

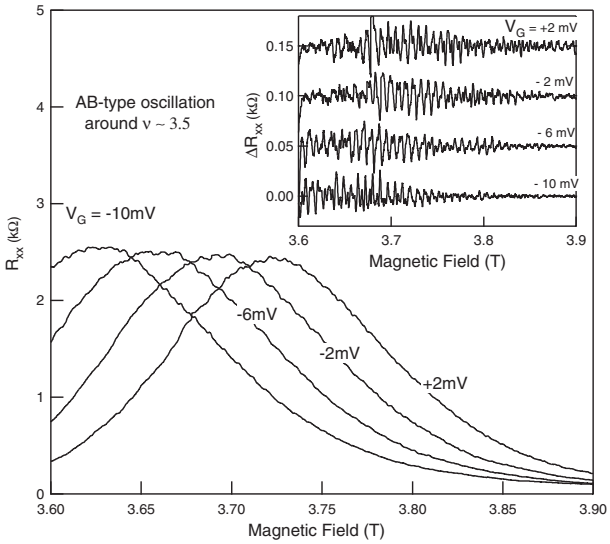

Fig. 5. Magnetoresistance of sample #2 at higher magnetic field. The AB-type oscillation is superimposed on the resistance peak in the quantum Hall plateau transition region between $\nu = 4$ and 3 for different settings of the gate voltage. The inset shows the oscillatory part.

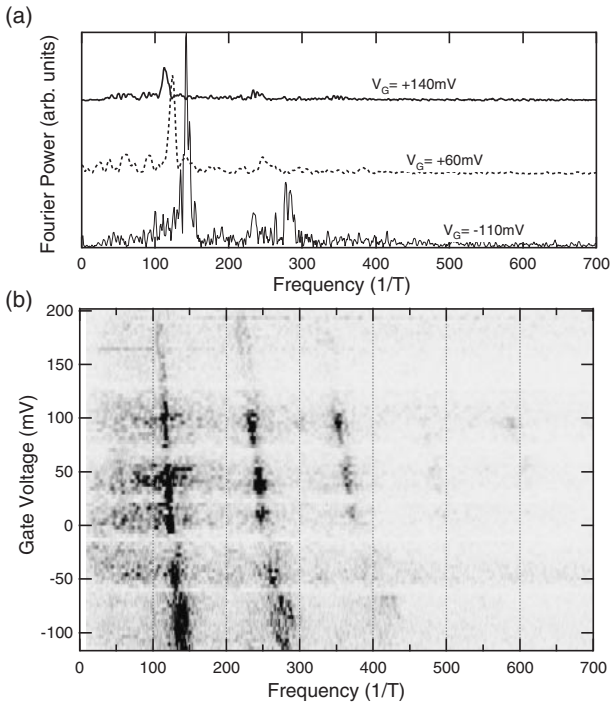

Fig. 6. (a) Fourier power spectra of the high-field AB-type oscillation in sample #2 at $\nu \sim 3.5$ for different values of V_G. (b) Gray scale plot showing the global evolution of the Fourier spectum as a function of the gate voltage.

electron density), the oscillation frequency increases, i.e., the effective loop area increases. In Fig. 6(b), the HFABO period changes from $\Delta B = 8.7$ mT at $V_G = +200$ mV to 7.2 mT at -110 mV. The corresponding values of effective antidot diameter are $d^* = 690$ and 760 nm, respectively. Two factors contribute to the change in the effective diameter. One is an increase in the width of depletion region around antidot with decreasing electron density. The other is the fact that the outermost edge channel is farther

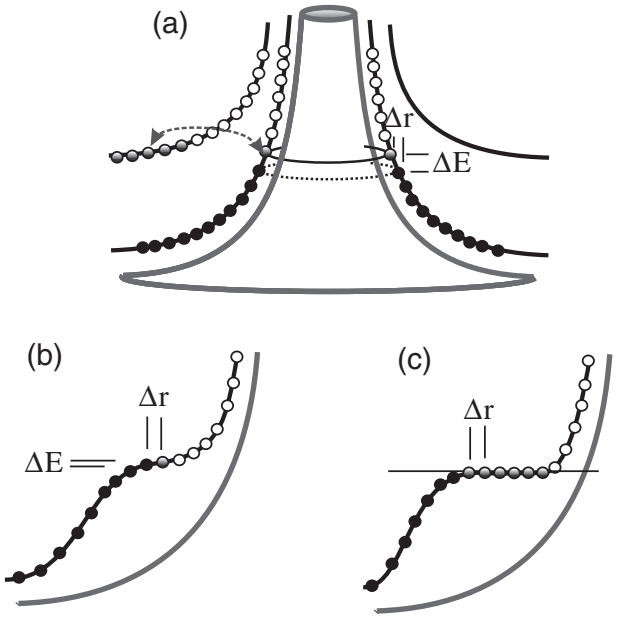

Fig. 7. (a) Single particle states encircling the antidot. The solid and open dots represent occupied and unoccupied states, respectively. Although not shown in this figure, there exist, in general, multiple edge states depending on the value of filling factor ν. In the quantum Hall plateau transition regime, there is also an extended state in the bulk region. The outermost edge state couples with the extended state via tunnelling. The pictures in panel (b) and (c) takes into account self-consistent screening. In (b), screening is not perfect so that there is a finite potential gradient albeit much smaller than the bare potential gradient. In (c), a ring of compressible electron liquid is formed around the antidot and the local potential is flat.

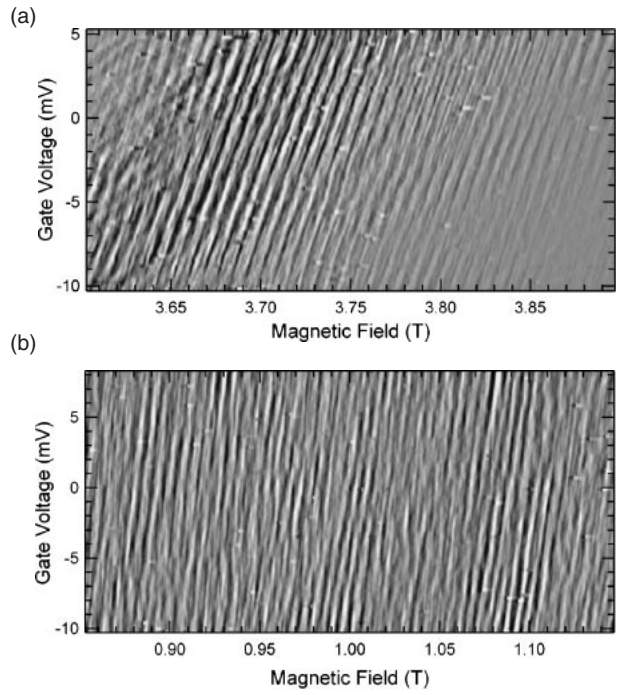

Fig. 8. Gray scale plot of the high-field AB-type oscillation at different ranges of filling factor; (a) $\nu \sim 3.5$, (b) $\nu \sim 11$. White represents higher resistance. Note the difference in the rate of phase evolution with gate votage.

Table I. Comparison of ΔB and ΔV_G in different field ranges. The numbers following the $\pm$ sign in the ΔB column represent the half width of the Fourier peak.

V_G (mV)	n_e ($\times 10^{15}$ m^{-2})	B (T)	ν	ΔB (mT)	ΔV_G (mV)
0	2.9	1	12–10	5.7 ± 0.8	6.3
		2.5	6–4	7.1 ± 0.5	4.2
		3.7	4–3	7.5 ± 0.4	2.5
		4.9	3–2	7.9 ± 0.3	2.0
−60	2.4	3.4	~3	7.4 ± 0.2	1.7

away from the antidot periphery for lower magnetic field. (Since the filling factor $\nu \sim 3.5$ is fixed in Fig. 6, lower electron density implies lower magnetic field range.) Figure 6 also shows the trend that the oscillation amplitude becomes larger as the conducting channels between antidots are narrowed by applying more negative gate bias.

The basic mechanism of HFABO is understood on the basis of a picture given in Fig. 7 which illustrates the edge states formed around an antidot in the quantum Hall regime. Single particle states localized around each antidot are quantized so as to enclose an integer number of flux quanta. As the magnetic field is swept, these single particle states pass through E_F one by one, giving rise to periodic change in the state at the Fermi energy. In the qunatum Hall plateau transition regime, percolating extended states run through the bulk of the system which couples with the edge states around antidots via tunnelling. In this situation, periodic change in the edge state at E_F is manifested as the AB-type oscillation in the macroscpic transport in the system.

From the picture in Fig. 7, it is readily anticipated that periodic crossing of single particle states through E_F can be also induced by sweeping V_G. Figure 8 shows evolution of magnetoresistance oscillation with V_G as gray scale plot. Notice that the range of V_G shown in this figure is only a small part of the whole range of V_G shown in Fig. 6, so that the period of HFABO does not change in this range. The slanted stripe patterns in these gray scale plot indicate that the phase of the AB oscillation is shifted as V_G is changed.

Figures 8(a) and 8(b) clearly show that the rate of phase evolution with V_G differs substantially from one field range to another. The dependence is summarized in Table I which gives the values of the HFABO period at different field ranges and different gate voltages. Both the AB period ΔB and the period in the gate voltage ΔV_G are given.

In what follows, we discuss the physical origin of the dependences of ΔB and ΔV_G on B and V_G. The single particle states around an antidot depicted in Fig. 7(a) obey the following flux quantization condition.

$$\pi r^2 B = n \frac{h}{e} \quad (n\text{: integer}), \tag{1}$$

where r is the radius of the circular orbit of a single particle state at the Fermi level. The difference of radii between two successive circular orbits is

$$\Delta r = \frac{h}{2\pi reB} \approx \frac{h}{\pi d^* eB}. \tag{2}$$

Figure 7(a) depicts these single particle states for non-interacting electrons, i.e., disregarding the screening effect. In this picture, the energy separation between two adjacent

quantized states is given by

$$\Delta E = \left(\frac{\mathrm{d}V}{\mathrm{d}r}\right)\Delta r = \frac{h}{\pi d^* eB}\left(\frac{\mathrm{d}V}{\mathrm{d}r}\right), \tag{3}$$

where $(\mathrm{d}V/\mathrm{d}r)$ denotes the slope of the antidot potential.

Let us first focus on the behavior of ΔB given in the second last column of Table I. We note that the AB period corresponding to the geometrical area of antidots (diameter $d = 670\,\mathrm{nm}$) is 11.7 mT. The values of $\Delta B = 7.1$ to 7.9 mT obtained in the quantum Hall regime are considerably smaller. These values indicate that the effective diameter d^* of antidots is larger by ~150 to 190 nm, depending on the field range. The difference comes from the width of depletion ring and the position of the relevant edge channel. As seen in Table I, ΔB is smaller for lower magnetic fields, which implies larger effective area. This is consistent with the picture that the relevant edge channel (i.e., the outermost one) is farther away from the antidot edge.

In the magnetic field range $B \sim 1\,\mathrm{T}$, the observed period 5.7 mT is much closer to the value 5.2 mT for the LFABO. This field range belongs to the Shubnikov–de Haas regime, so that the edge picture is of marginal relevance. The behavior in this field range should be regarded as a crossover between LFABO and HFABO.

Next we turn to the variation of ΔV_G with B and V_G, given in the last column of Table I. Here, detailed spectral structure of the single particle states is essential. The experimentally obtained values of ΔV_G differ substantially depending on the field range. The primary cause of this dependence lies in eq. (3), which contains B in the denominator. Namely, the spatial separation between two adjacent single particle states is smaller for higher field. Hence the corresponding energy separation is smaller, which results in more rapid oscillation when V_G is swept. A more quantitative comparison requires conversion from δV_G to the chemical potential shift $\delta\mu$, and also a detailed account of the potential slope $(\mathrm{d}V/\mathrm{d}r)$.

The amount of chemical potential shift $\delta\mu$ induced by a change in the gate bias V_G is given by a conversion factor $\alpha = \mathrm{d}\mu/\mathrm{d}V_\mathrm{G}$. Its value at zero magnetic field is given by

$$\alpha = \frac{C}{eD_0} = \frac{C}{e}\frac{2\pi\hbar^2}{m^*}, \tag{4}$$

where C denotes the capacitance between the gate and 2DEG and $D_0 = m^*/(2\pi\hbar^2)$ is the density of states. The value of α at zero magnetic field can be obtained from the n-versus-V_G relation shown in the inset of Fig. 2. In high magnetic fields, α can differ significantly from its zero field value owing to Landau quantization of the spectrum. Particularly in the quantum Hall states, where bulk states become incompressble, α is strongly modified. In the quantum Hall plateau transition region, where bulk states are delocalized, we expect that the qualitative behavior of α is similar to the zero field case. If we use $\alpha = 0.023$ for $V_\mathrm{G} = 0\,\mathrm{mV}$, the observed value of $\Delta V_\mathrm{G} = 2.0\,\mathrm{mV}$ for $B = 4.9\,\mathrm{T}$ is translated to $\Delta\mu = 46\,\mu\mathrm{eV}$.

The V_G-dependence of ΔV_G shown in Table I can be simply understood as due to the V_G-dependence of the convsersion factor α. For the present sample, $\alpha = 0.023$ and 0.033 for $V_\mathrm{G} = 0\,\mathrm{mV}$ and $-60\,\mathrm{mV}$, respectively, as can be calculated from the local slope of the curve shown in the inset of Fig. 2. The observed values, $\Delta V_\mathrm{G} = 2.5$ and 1.7 mV for $V_\mathrm{G} = 0$ and $-60\,\mathrm{mV}$ at roughly the same field range $B \sim 3.5\,\mathrm{T}$, are then both translated to the same value of chemical potential shift $\Delta\mu = 57\,\mu\mathrm{eV}$, when multiplied with the conversion factors.

On the other hand, the absolute values of $\Delta\mu$ calls for interpretation based on the detailed model of the realistic potential profile. A rough estimate of the bare potential from the values of band gap and the width of depletion region yields $(\mathrm{d}V/\mathrm{d}r)$ on the order of a few $\mathrm{V}/\mu\mathrm{m}$. This would give an energy separation between two adjacent single particle states on the order of 1 meV for $B \sim 5\,\mathrm{T}$. The experimental $\Delta\mu$, as obtained from the ΔV_G data and the conversion factor is clearly much smaller, indicating that the naive estimation based on a non-interacting model is widely off the mark. Thus we have to take into account the fact that the effective electrostatic potential at the edge of a quantum Hall system is greatly modified by self-consistent screening effect[20] as illustrated in Figs. 7(b) and 7(c). The potential gradient is almost exclusively supported by the incompressible region and the potential in the compressible region becomes much flatter than the bare potential [Fig. 7(a)]. Figures 7(b) and 7(c) represent two different models of the edge state formed around the antidot, which have been proposed in the context of single antidot experiments.[21–24] The interpretation of the experimentally obtained ΔV_G (or $\Delta\mu$) depends critically on which of the two models to stand upon.

Figure 7(b) represents a case in which screening is incomplete so that the slope is small but still finite. According to the picture of Fig. 7(b),[22,24] $\Delta\mu$ reflects the gradient of the screened potential which is far smaller than the slope of the bare potential but is still nonzero. By contrast, according to the picture of Fig. 7(c), in which the screened potential is thought to be flat,[21,23] $\Delta\mu$ originates from charging energy of the compressible ring. Which of the two models is more appropriate is currently controversial in the context of single antidot experiments.[21–24] Likewise, it is difficult at the moment to judge which is more appropriate for the present system of antidot lattice.

In order to gain insight into this issue, it is crucial to pay attention to the amplitude of the HFABO in the unit of e^2/h. The conductance oscillation amplitude of the presently observed HFABO is typically $\sim(0.01\text{–}0.05)(e^2/h)$. This is smaller in magnitude to those typically observed in single antidot systems.[21–24] However, considering the various factors that may act to reduce the amplitude, such as ensemble avaraging, lithographical fluctuation, random potential, decoherence, this value of AB oscillation amplitude is thought to be *fairly large*. Indeed, if 10^4 rings behave literally incoherently, the amplitude would be diminished by two orders of magnitude. In reality, coherent region may cover several or several tens of rings, but still amplitude reduction would be substantial.

Firstly, this is relevant to a basic question, "Does the observed HFABO come from the entire part of the antidot lattice, or from a specific part (for example those near the edge of the Hall bar)?". The fact that the amplitude of the HFABO does not change so sensitively with the gate voltage, seems to suggest that it is unlikely to originate only from a specific part of the sample, but that essentially the

whole regions of the sample participate to the osillatory resistance change. Another support to this view comes from the fact that the oscillation is most conspicuous in the quantum Hall plateau transition region, where transport current is spread over the bulk of the 2DEG sample. This is currently an issue open to future investigations. We may gain a useful piece of information by investigating, for instance, the dependence of the AB amplitude on the overall sample size, which we plan to do.

If the HFABO indeed arises from the whole system, however, it raises another basic question how the contributions from individual antidots add up at least partially coherently. Since crossing of single particle states through E_F is generally thought to occur incoherently among individual antidots, the *fairly large* amplitude observed in the experiment seems to call for some sort of mechanisms that tends to retain global coherence over the otherwise incoherent processes at individual antidots. In this context, it seems more difficult to devise such a mechanism based on the model of Fig. 7(b) than Fig. 7(c). In the latter case, where the phenomenon is attributed to Coulomb oscillation effect, one may argue for correlation among tunneling processes at different antidots, although admittedly there is no concrete model for such correlation.

3.3 Temperature dependence of the oscillations

Let us now turn to the issue of decoherence. All the three types of oscillation lose their amplitude with increasing temperature. Figure 9(a) shows the oscillatory part of low-field magnetoresistance in sample #2 at different temperatures for $V_G = 0$. It is seen that the AB-type oscillation diminishes more rapidly with temperature than the AAS oscillation. The temperature dependences of the oscillation amplitude were obtained from the Fourier spectrum, both for the fundamental component and the higher harmonics. Figures 9(b) and 9(c) summarize the temperature dependences of the AAS and AB-type oscillation amplitude.

The temperature dependence of the AAS oscillation amplitude can be expressed as

$$A^{\mathrm{AAS}}_{(2e)} \propto \mathrm{e}^{-L/L_\phi} \propto \mathrm{e}^{-(T/T^*_{\mathrm{AAS}})^p}, \tag{5}$$

where L_ϕ denotes the phase coherence length and L is an appropriate length scale on the order of the loop size. The parameter T^*_{AAS} represents a charecteristic temperature scale of decoherence. The phase coherence length is $L_\phi = v_F\tau_\phi$ (v_F being the Fermi velocity) in a ballistic system. In most cases, phase relaxation at low temperature is governed by electron-electron scattering, and the dephasing time is given by $\tau_\phi \propto T^{-p}$ with exponent p dependent on the dimensionality and disorder of the system. In ballistic 1D system, $\tau_\phi \propto T^{-1}$, so that $L_\phi \propto T^{-1}$. Such behavior is experimentally observed in ballistic single ring systems with small number of 1D channels.[14,15] As for the present system, fitting eq. (5) to the experimental results yields $p \sim 1.5$ for sample #1 and $p \sim 1.1$ for #2. These values lie between $L_\phi \propto T^{-2}$ for 2D system and $\propto T^{-1}$ for 1D system.[25] Note that sample #1 with smaller aspect ratio has a larger number of conducting channels between antidots, so that is closer to 2D system.

Higher harmonic components (such as $h/4e$ and $h/6e$) correspond to multiple turns around the loop. The corresponding Fourier amplitude is expected to follow

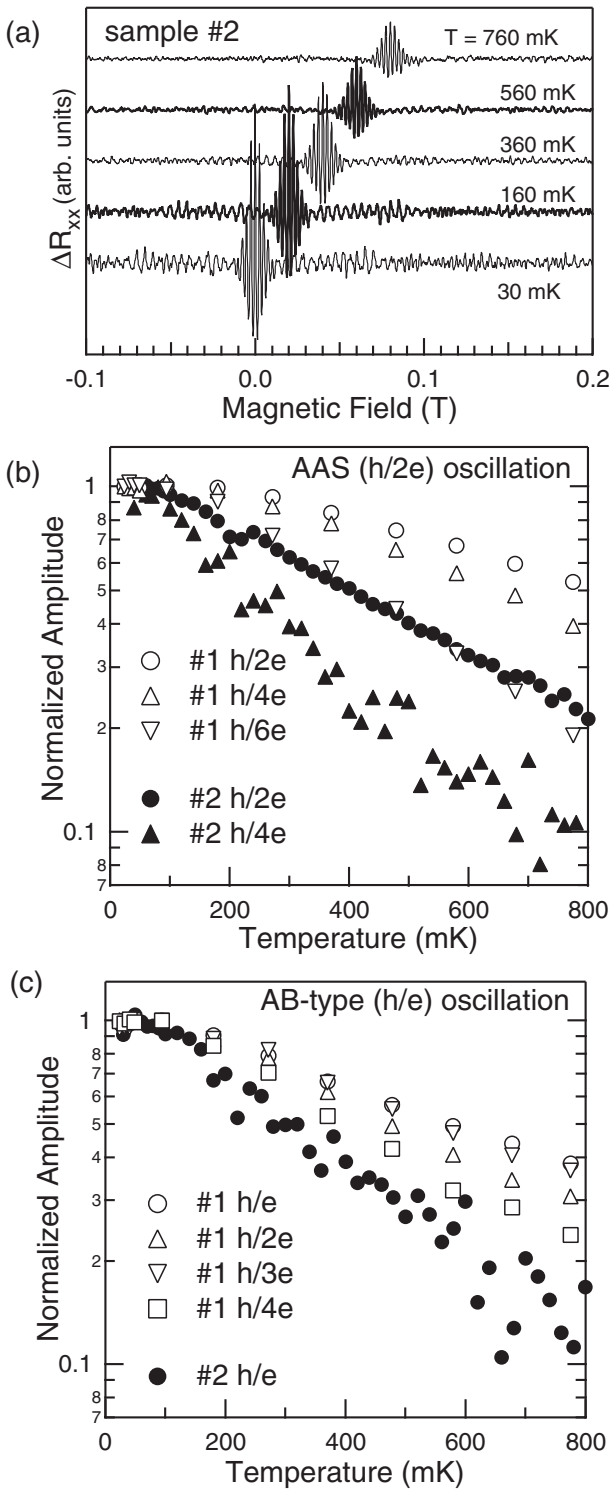

Fig. 9. (a) Oscillatory part of low field magnetoresistance in sample #2 at different temperatures. Each trace is shifted both vertically and horizontally for clarity. (b) Temperature dependence of the amplitude of the AAS oscillation. (c) Temperature dependence of the amplitude of the low-field AB-type oscillation.

$$A^{\mathrm{AAS}}_{(4e)} \propto \left[A^{\mathrm{AAS}}_{(2e)}\right]^2, \quad A^{\mathrm{AAS}}_{(6e)} \propto \left[A^{\mathrm{AAS}}_{(2e)}\right]^3. \tag{6}$$

The experimental results shown in Fig. 9(b) obeys these relations. The phase coherence length L_ϕ estimated from the ratios of the harmonic components is on the order of a few μm, and saturates at the lowest temperatures. Saturation of the AAS oscillation at low temperature is more conspicuous

for large negative gate bias (lower carrier density).

The behavior of the AB-type oscillation shown in Fig. 9(c) is more difficult to interpret. The temperature dependences of the harmonic components do not obey such a simple scaling relation as the AAS case. The T-dependence of the LFABO is found to follow

$$A_{(e)}^{\mathrm{LFABO}} \propto \mathrm{e}^{-T/T^*_{\mathrm{LFABO}}}, \tag{7}$$

with the value of characteristic temperature T^*_{LFABO} smaller for the sample with larger aspect ratio.

If the AB-type oscillation is considered as simple manifestation of oscillatory fine structure of a fixed density of state profile with characteristic energy scale ΔE, the expected temperature dependence is

$$A \propto \frac{aT}{\sinh aT}, \quad a = \frac{2\pi^2 k_{\mathrm{B}}}{\Delta E} \tag{8}$$

similar to the temperature dependence of Shubnikov–de Haas effect. Equation (8) predicts a saturating behavior below the temperature corresponding to $\Delta E/2\pi^2 k_{\mathrm{B}}$.

Open and solid circles in Fig. 10 shows the measured temperature dependence of the LFABO amplitude for samples #1 and #2. Dashed curves represent fitting of eq. (8) to the experimental data at higher temperatures. It is clear that the data points at low temperatures stay above the dashed curves.

In the present case, the overall system size L_{sys} is much larger than the phase coherence length L_ϕ, so that the system can be regarded as consisting of $N = (L_{\mathrm{sys}}/L_\phi)^2$ independent parts. Since L_ϕ is temperature dependent, this introduces an extra factor in temperature dependence through the ensemble averaging. We express $L_\phi(T)$ as

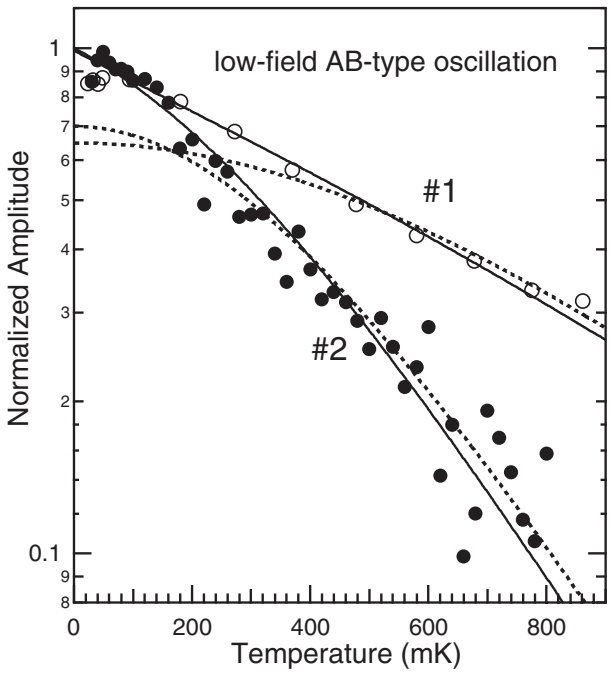

Fig. 10. Temperature dependence of the amplitude of LFABO in samples #1 and #2. The dashed curves represent eq. (8) with fitting parameter $\Delta E = 7.3\,\mathrm{K}$ for #1 and $\Delta E = 3.9\,\mathrm{K}$ for #2. The solid curves represent eq. (10) with $p = 1$. The values of other fitting parameters are $\Delta E = 9.8\,\mathrm{K}$ and $T_0 = 0.7\,\mathrm{K}$ for #1, and $\Delta E = 4.3\,\mathrm{K}$ and $T_0 = 0.7\,\mathrm{K}$ for #2, respectively.

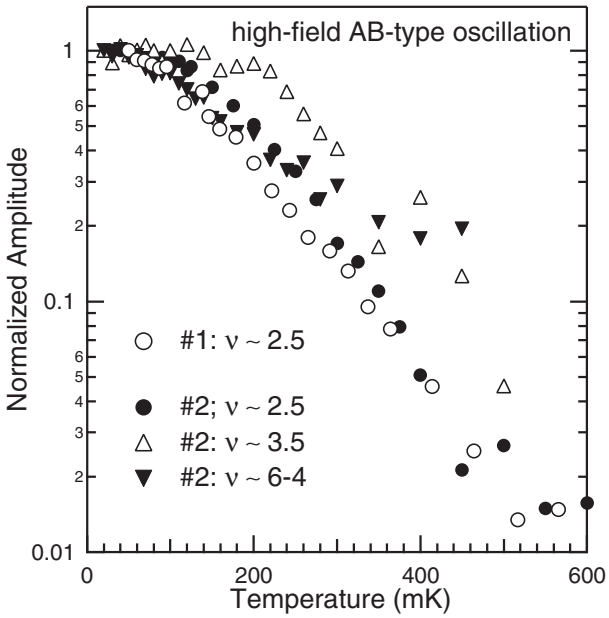

Fig. 11. Temperature depenedence of the amplitude of HFABO in different magnetic field ranges.

$$L_\phi(T) \propto (T + T_0)^{-p}, \tag{9}$$

which interpolates T^{-p} behavior at higher temperature and saturation at low temperature. Multiplying eq. (8) with a factor $N^{-1/2} = L_\phi/L_{\mathrm{sys}}$ gives

$$A_{(e)}^{\mathrm{LFABO}} \propto \left(\frac{T_0}{T + T_0}\right)^p \frac{aT}{\sinh aT}. \tag{10}$$

The solid curves in Fig. 10 show the fitting of the above expression (assuming $p = 1$ for simplicity), which give semiquantitative account of the experimental data.

Figure 11 presents the temperature dependence of the amplitude of HFABO in different field ranges. The observed behavior turns out to be rather complex and does not allow quantitative analysis. Nevertheless, it is noted that the slope in the higher temperature range is larger for higher magnetic fields (lower ν values). This is consisitent with eq. (8), because, according to the discussion in the preceeding subsection, the spatial separation Δr between two adjacent single particle states is smaller for higher field, which tends to make ΔE smaller. On the other hand, the saturation behavior at low temperature does not appear systematic and cannot be explained in any simple model.

4. Conclusions

We have studied three different types of quantum oscillations in macroscopic samples of triangular antidot lattice, i.e., AAS and AB-type oscillations near zero magnetic field and AB-type oscillation in the quantum Hall plateau transition regime at high fields. For the AAS and LFABO, the oscillation period is determined by the unit cell size, while that of the HFABO is governed by the size of the antidot. The HFABO originates from quantization of single particle states circumnavigating the antidot. In particular, the rate of phase evolution with the gate voltage (chemical potential) furnishes the information on the nature of the self-consistent potential for the edge states. Whether the

observed period ΔV_G (or $\Delta\mu$) should be attributed to a finite slope of the incompletely screened potential, or to the Coulomb charging effect, remains to be elucidated. The fairly large amplitude of the HFABO seems to call for some sort of mechanism that brings coherent contributions from individual antidots, which is unknown at the moment. The temperature dependence of the AAS effect in antidot lattice is understood basically in the same way as the single ring case in terms of phase coherence length. The temperature dependence of the AB-tye oscillation deviates from a simple model assuming a prefixed oscillatory fine structure in the density of states. A phenomenological model incorporating the condition that the total system size is much larger than the phase coherence length, gives a reasonable account of the observed temperature dependence.

Acknowledgement

This work has been supported by a Grant-in-Aid for COE Research "Quantum Dot and Its Application" (#12CE2004), and by a Grant-in-Aid for Scientific Research (#13304025), from the Ministry of Education, Culture, Sports, Science and Technology (MEXT), Japan.

1) Y. Aharonov and D. Bohm: Phys. Rev. **115** (1959) 485.
2) D. Yu. Sharvin and Yu. V. Sharvin: Pis'ma Zh. Eksp. Theor. Fiz. **34** (1981) 285 [JETP Lett. **34** (1981) 272].
3) B. L. Altshuler, A. G. Aronov and B. Z. Spivak: Pis'ma Zh. Eksp. Theor. Fiz. **33** (1981) 101 [JETP Lett. **33** (1981) 94].
4) R. A. Webb, S. Washburn, C. P. Umbach and R. B. Raibowitz: Phys. Rev. Lett. **54** (1985) 2696.
5) S. Datta, M. R. Mellock, S. Bandyopadhyay, R. Norem, M. Vazirir, M. Miller and R. Reifenberger: Phys. Rev. Lett. **55** (1985) 2344; G. Timp, A. M. Chang, J. E. Cunningham, T. Y. Chang, P. Mankiewich, R. Behringer and R. E. Howard: Phys. Rev. Lett. **58** (1987) 2814.
6) F. Nihey and K. Nakamura: Physica B **184** (1993) 398.
7) D. Weiss, K. Richter, A. Menshing, R. Bergmann, H. Schewzer, K. von Klitzing and G. Weimann: Phys. Rev. Lett. **70** (1993) 4118.
8) F. Nihey, S. W. Hwang and K. Nakamura: Phys. Rev. B **51** (1995) 4649.
9) C. P. Umbach, C. van Haesendonck, R. B. Laibowitz, S. Washburn and R. A. Webb: Phys. Rev. Lett. **56** (1986) 386.
10) T. Ando, S. Uryu, S. Ishizaka and T. Nakanishi: Choas, Solitons & Fractals **8** (1997) 1057; T. Ando: in *Mesoscopic Physics and Electronics*, ed. T. Ando *et al.* (Springer, Heidelberg, 1998) p. 72.
11) S. Ishizaka, F. Nihey, K. Nakamura, J. Sone and T. Ando: Phys. Rev. B **51** (1995) 9881.
12) S. Uryu and T. Ando: Phys. Rev. B **53** (1996) 13613.
13) R. Schuster, K. Ensslin, D. Wharam, S. Kühn, J. P. Kotthaus, G. Böhm, W. Klein, G. Tränkle and G. Weimann: Phys. Rev. B **49** (1994) 8510.
14) A. E. Hansen, A. Kristensen, S. Pedersen, C. B. Sorensen and P. E. Lindelof: Phys. Rev. B **64** (2001) 045327.
15) K. Kobayashi, H. Aikawa, S. Katsumoto and Y. Iye: J. Phys. Soc. Jpn. **71** (2002) 2094.
16) C. Albrecht, J. H. Smet, D. Weiss, K. von Klitzing, R. Hennig, M. Langenbuch, M. Shurke, U. Rössler, V. Umansky and H. Schweizer: Phys. Rev. Lett. **83** (1999) 2234.
17) C. Albrecht, J. H. Smet, K. von Klitzing, D. Weiss, V. Umansky and H. Schweizer: Phys. Rev. Lett. **86** (2001) 147.
18) A. Pouydebasque, A. G. Pogosov, M. V. Budantsev, A. E. Plotnikov, A. I. Toropov, D. K. Maude and J. C. Portal: Phys. Rev. B **66** (2002) 035324.
19) P. D. Ye, L. W. Engel, D. C. Tsui, J. A. Simmons, J. R. Wendt, G. A. Vawter and J. L. Reno: Phys. Rev. B **65** (2002) 121305.
20) D. B. Chklovskii, B. I. Shklovskii and L. I. Glazman: Phys. Rev. B **46** (1992) 4026.
21) C. J. B. Ford, P. J. Simpson, I. Zailer, D. R. Mace, M. Yosefin, M. Pepper, D. A. Ritchie, J. E. F. Frost, M. P. Grimshaw and G. A. C. Jones: Phys. Rev. B **49** (1994) 17456.
22) I. J. Massilta and V. J. Goldman: Phys. Rev. B **57** (1998) R4273.
23) M. Kataoka, C. J. B. Ford, G. Faini, D. Mailly, M. Y. Simmons, D. R. Macd, C.-T. Liang and D. A. Ritchie: Phys. Rev. Lett. **83** (1999) 160.
24) I. Karakurt, V. J. Goldman, J. Liu and A. Zalsvsky: Phys. Rev. Lett. **87** (2001) 146801.
25) J. J. Lin and J. P. Bird: J. Phys.: Condens. Matter **14** (2002) R501.